FLIGHT DYNAMICS OF A MARS HELICOPTER*

Håvard Fjær Grip*, Wayne Johnson**, Carlos Malpica**, Daniel P. Scharf*, Milan Mandić*, Larry Young**, Brian Allan†, Bérénice Mettler‡, and Miguel San Martin*

*Jet Propulsion Laboratory, California Institute of Technology, Pasadena, CA
**NASA Ames Research Center, Moffet Field, CA
†NASA Langley Research Center, Hampton, VA
‡University of Minnesota, Aerospace Engineering and Mechanics, Minneapolis, MN

Abstract

Helicopters have the potential to transform Mars exploration by providing a highly mobile platform for forward reconnaissance as an aid for ground-based systems. NASA is therefore considering the possibility of sending a small helicopter to the Martian surface as part of a future mission. Helicopter flight on Mars is challenging due to the extremely thin atmosphere, which is only partially offset by a reduction in gravity. In this paper we focus on flight dynamics and controllability issues for the proposed Mars Helicopter, in particular the areas in which the dynamics departs from typical behavior on Earth. We discuss insights gained from modeling and simulation as well as system identification performed with a test vehicle in the relevant atmospheric condition, which culminated in the first demonstration of controlled helicopter flight in Martian atmospheric conditions in May 2016.

1 Introduction

Starting with the first attempted flybys of Mars in the 1960s, human exploration of the Red Planet has evolved through ever-more sophisticated means, with the use of orbiters, stationary landers, and more recently rovers that have traveled over distances of tens of kilometers in search of new knowledge. Yet, despite discussion since the early days of space exploration, no mission has so far attempted to unlock the *aerial* dimension of Mars exploration through the use of atmospheric flyers.

This could be about to change, as NASA is considering the possibility of sending a small helicopter to the Martian surface as part of a future mission, as a *technology demonstration* to verify the feasibility and utility of using helicopters for future Mars exploration.

The use of helicopters promises to bridge a *resolution gap* in current Mars exploration capabilities—between orbiters providing large-area imagery at low resolution, and rovers that provide detailed imagery limited by line-of-sight from the current rover location. Paired with a rover, a helicopter can act as a forward reconnaissance platform, helping to identify promising science targets or mapping the terrain ahead of the rover. Looking further ahead, helicopters may one day carry their own science payloads to areas that are inaccessible to rovers.

*The work of H. F. Grip, D. P. Scharf, M. Mandić, and M. San Martin was carried out at the Jet Propulsion Laboratory, California Institute of Technology, under a contract with the National Aeronautics and Space Administration.

Figure 1: Artist's concept of the proposed Mars Helicopter.

1.1 Challenges of Mars Helicopter Flight

Like any spacecraft or spacecraft instrument, a helicopter designed for Mars faces a host of challenging requirements not typically seen on Earth: it must withstand high structural loads during launch, extreme temperature variations, high levels of radiation, and be vacuum compatible; it must satisfy cleanliness requirements related to planetary protection; and it must operate entirely without physical intervention after launch. It must also be compactly designed and safely deployable after landing.

In this paper, we focus on a different set of challenges, namely, those related to the *flight dynamics* of the vehicle when operating in the Martian environment, and how these affect the mechanical design of the vehicle and the flight control algorithms. Two aspects of the environment are primary drivers for the flight dynamics of a helicopter on Mars:

- *Atmosphere*: the Martian atmosphere consists primarily of CO_2 at ***only 1–2% of Earth's atmospheric density*** at sea level, equivalent to altitudes of approximately $100,000$ ft on Earth.
- *Gravity*: the Martian gravity is approximately 38% of Earth's gravity.

The most obvious effect of the reduced density is a reduction in lift capability for any given rotor. The reduced gravity, while helpful, does not nearly make up for this reduction in lift. Beyond this, the Martian environment also influences the helicopter flight dynamics in less obvious but highly consequential ways, which ultimately influence both the design of the helicopter itself and the algorithms used to control it.

© 2017. All rights reserved.

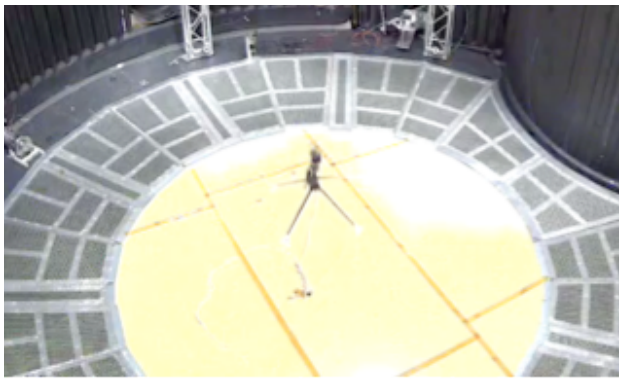

Figure 2: In this image, the Mars Helicopter demonstration vehicle is taking off for the first controlled flight in Martian atmospheric conditions, inside JPL's 25-ft Space Simulator.

Designing a helicopter for Mars also presents serious challenges in terms of testing, verification, and validation. It is not practically possible to fully replicate the Mars environment on Earth; this forces a greater reliance on analysis, modeling, and simulation than for a typical small-scale rotorcraft program on Earth, combined with limited testing in partially replicated environments.

1.2 Controlled-Flight Demonstration

In May 2016, the Mars Helicopter project conducted the first-ever controlled helicopter flight in Martian atmospheric conditions, in the 25-ft Space Simulator at NASA's Jet Propulsion Laboratory. The demonstration vehicle was a co-axial helicopter featuring a 1.21-m diameter rotor—the same size being considered for Mars flight—rotating at a speed of 2600 RPM (see Figures 2 and 4). The vehicle was built by *AeroVironment, Inc.*, the primary industry partner on the Mars Helicopter project. Because the vehicle had to lift its own weight on Earth, it did not carry batteries or an avionics computing platform, but was connected to a ground station via power and data tethers hanging below the vehicle.

The flight demonstration followed an intensive vehicle design effort that was driven by analysis of the flight properties of helicopters on Mars. Moreover, due to a high degree of modeling uncertainty and the almost complete lack of prior work on flight dynamics in Mars-like conditions, a *system identification* program was executed to identify the actual dynamics of the vehicle as-built, thereby casting further light on the unique properties of Mars helicopters.

1.3 Topics of this Paper

In this paper we focus on flight dynamics and controllability issues for the Mars Helicopter, in particular the areas in which the Mars Helicopter dynamics departs from typical behavior on Earth. The following areas are covered specifically:

- overview of the Mars Helicopter vehicle design
- modeling of Mars Helicopter flight dynamics
- impact of low density on flap dynamics in the Martian environment, and consequences for control and vehicle design
- sensitivity to edgewise flow
- low-frequency dynamics, including *apparent inertia* effects due to rotor flapping
- helicopter stability properties
- additional insights from system identification in Martian atmospheric conditions

We end with some concluding remarks on remaining work in the flight dynamics area for the proposed Mars Helicopter.

1.4 Previous Work on Mars Rotorcraft

Although aerial vehicle concepts for Mars have been proposed since the earliest days of space exploration, the full challenges of flight in the extremely thin, cold, and primarily CO_2-based atmosphere of Mars only become apparent after the Viking Lander missions of the 1970s. For approximately two decades afterwards only Mars airplane concepts were studied. Savu and Trifu [12] were among the first to consider the design implications of Mars rotorcraft; however, their work was not carried forward beyond its initial study.

In 2000, Stanford University and JPL, as a tangential offshoot of Stanford's NASA NIAC-sponsored micro-rotorcraft work attempted a proof-of-concept test of a small rotor under Mars-like atmospheric conditions in a JPL vacuum chamber [7]. No experimental results were published from this initial proof-of-concept test, though video was released at the time. Independently, at approximately the same time, a series of papers were published by NASA Ames Research Center studying the technical challenges of various Mars rotorcraft configurations and other vertical lift planetary aerial vehicles [1, 18, 24, 20].

In 2000, Sikorsky Aircraft and NASA Ames Research Center co-sponsored the AHS International Student Design Competition on the topic of a Mars rotorcraft. Thompson [15] and Datta et al. [3] are summary papers describing respectively the Georgia Tech and University of Maryland Mars rotorcraft design entries. In 2002, the first experimental results for a rotor hover test under Mars-like conditions were published [26]. Over the next decade-and-a-half, papers continued to be occasionally published by NASA Ames [19, 25, 21, 22, 23] on the topic of planetary aerial vehicles, both fixed-wing and vertical lift aerial vehicles.

As time went on, interest slowly grew, and papers by other authors, organizations, and countries began to be published on Mars rotorcraft and vertical lift planetary aerial vehicles [17, 13]. In 2014, JPL and AeroVironment published an initial paper on what would ultimately become the conceptual foundation for the current Mars Helicopter effort [2]. The concept has significantly evolved over the past few years, but retains many of its core features.

Although several of the papers cited were concerned with feasibility of Mars rotorcraft from the point of view of thrust generation and power consumption, they did not address the flight dynamics or the design of closed-loop control for Mars rotorcraft at a detail level.

2 Vehicle Overview

The current Mars Helicopter baseline design features a co-axial rotor, with two counter-rotating, hingeless, 2-bladed ro-

© 2017. All rights reserved.

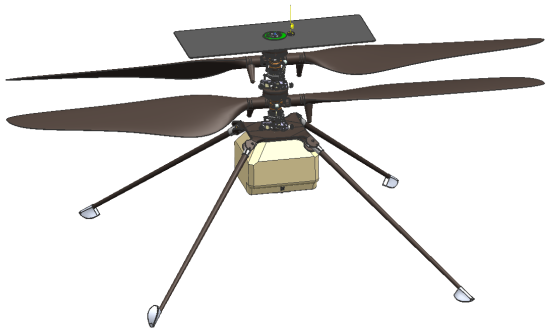

Figure 3: CAD drawing of the proposed Mars Helicopter.

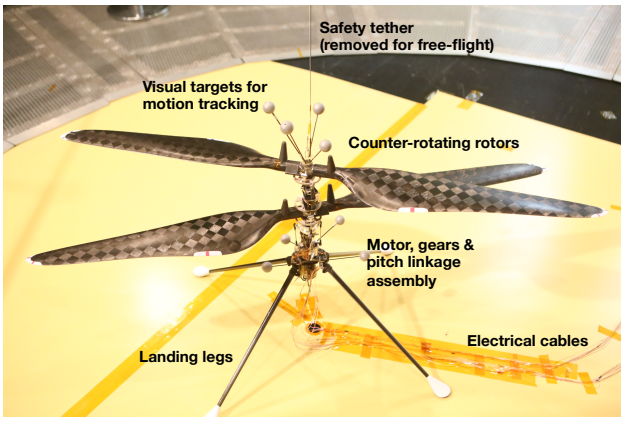

Figure 4: The demonstration vehicle used for controlled-flight demonstration in Martian atmospheric conditions.

tors measuring 1.21 m in diameter, spaced apart by approximately 17% of the rotor radius. The rotors are designed to operate at speeds up to 2800 RPM. The speed is fixed for the duration of flight, depending primarily on the current density, which is in the range 0.014–0.02 kg/m^3. Control is via upper and lower swashplates, providing collective control with a total range of 22°, and cyclic control with a range of $\pm 10°$, for each rotor.

Within the allowable density range, the vehicle is designed to have the power and aerodynamic capability to achieve thrust levels of at least 40% above hover thrust before the onset of stall. The helicopter would only fly in favorable weather, with wind velocities limited to 9 m/s horizontally and 2 m/s vertically, with a maximum gust component of 3.5 m/s. Based on the forecasted weather, ground speed and climb/descent speeds would be limited such that maximum airspeed does not exceed 10 m/s horizontally and 3 m/s vertically.

The gross vehicle weight is less than 1.8 kg, a substantial portion of which is taken up by the batteries. The batteries provide energy for flights lasting up to 90 s, while also providing sufficient energy for non-flight operation of the onboard electronics and night-time survival heating. The batteries are rechargeable via a solar panel mounted on the non-rotating mast above the upper rotor. The batteries and other electronics are housed in a cube-like fuselage attached to the central mast, inside of which is a *warm electronics box* that is properly insulated and heated to protect against low night-time temperatures.

Flights would be conducted based on a flight plan uploaded from the ground, consisting of a series of waypoints. Due to the many minutes of communication delay between Earth and Mars, each flight must be conducted with full autonomy. For this purpose, onboard navigation is performed using a combination of a small, MEMS-based inertial measurement unit (IMU), a low-resolution downward-looking camera, and a laser rangefinder. The IMU, which measures accelerations and angular rates, is used for propagation of the vehicle state from one time step to the next. The camera is used together with the laser rangefinder to determine the height above ground and the translational velocity; this information is fused with the IMU solution. The onboard computation platform consists of a radiation-tolerant FPGA; a dual-redundant automotive-class microcontroller hosting the most critical flight control functions; and a cell-phone class processor hosting the vision-based navigation functions.

2.1 Demonstration Vehicle

The vehicle used to demonstrate controlled flight in JPL's 25-ft Space Simulator is shown in Figure 4. It featured a full-scale rotor similar to the intended Mars vehicle. However, since this vehicle was required to lift its own weight in Earth gravity, anything non-essential to the demonstration of controlled flight was left off the vehicle to reduce weight. Instead of onboard batteries, power was provided through an electrical tether hanging below the vehicle.

Unlike the proposed Mars vehicle, the flight demonstration vehicle was only equipped with cyclic control on the lower rotor. This provides sufficient degrees of freedom for control, but results in reduced control authority and greater cross-axis coupling due to asymmetry between the rotors.

For the demonstration vehicle, navigation was performed using a *Vicon* motion capture system, which determines both the position and attitude of the vehicle by tracking IR retroreflective targets on the vehicle using external cameras; this information was combined with an onboard IMU in a filter. The navigation algorithm and all other flight control functionality was hosted on a ground computer.

3 Modeling

The primary tool for studying flight dynamics for the proposed Mars Helicopter is the *Helicopter Control Analysis Tool* (*HeliCAT*), which was developed specifically for this purpose using the *Darts/Dshell* multibody simulation framework developed at JPL [see, e.g., 8]. The strength of this tool is that it is tailored toward needs in the guidance, navigation, and control area, with features including:

- detailed modeling of actuators and sensors, including camera imaging
- modeling of ground contact dynamics, including varied terrain and surface properties

© 2017. All rights reserved.

- modeling of ground support equipment, such as gimbals and force-torque sensors, for validation of the system identification approach
- flight software integration
- 3D visualization

In addition to generating models for control analysis, HeliCAT can be used to execute simulations of end-to-end missions with flight software in the loop.

The aircraft components are modeled in HeliCAT using rigid bodies connected by hinges. Other rotorcraft modeling tools offer higher-fidelity modeling of flexible bodies; these include CAMRAD II, a comprehensive analysis tool for rotorcraft that is widely used across NASA and in industry. CAMRAD II is used in the Mars Helicopter project to validate certain properties of HeliCAT and to perform higher-fidelity analysis related to thrust and power performance.

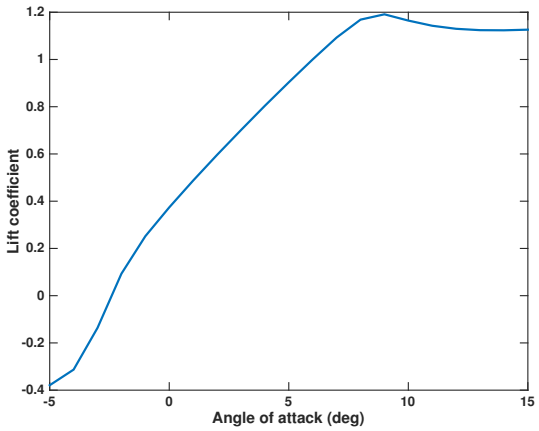

Figure 5: Typical plot of the lift coefficient as a function of angle-of-attack.

3.1 HeliCAT Modeling

The main bodies in the HeliCAT model are the fuselage, the mast, the blades, and the landing gear legs. The connection of the blades to the mast is configurable as a sequence of hinges with different properties, to represent different rotor designs.

3.1.1 Aerodynamic Forces

The aerodynamic forces on the blade are modeled by dividing the blade into a large number of slices with individual span, chord, twist, and sweep. Associated with each element is an airfoil table that tabulates the nondimensional coefficients of lift, drag, and pitch moment as a function of angle-of-attack and Mach number. The airfoil tables were generated by AeroVironment from two-dimensional CFD analysis of the specific blade section, using *ANSYS Fluent*. At each time step, forces and moments for each element are computed based on interpolating the airfoil data. Despite the low Reynolds number regime, the lift, drag, and moment characteristics are not dramatically different from typical characteristics at Earth densities; crucially for the flight dynamics, the lift curves exhibit a linear region as seen in Figure 5.

The two-dimensional airfoil tables only account for flow perpendicular to the quarter-chord of the blade. An estimate of radial drag effects due to yawed flow is included, based on the same airfoil tables [see 6, Ch. 6.22]. Tip losses are modeled by eliminating the lift and moment contribution (but not the drag) of the outermost portion of the blade. Unsteady aerodynamic effects are also included, based on the angular velocity and acceleration of the blade [see 6, Ch. 10.6].

Fuselage drag is modeled by a simple blunt-body drag model with no angle-of-attack dependency; due to the low density, this has little impact on the flight dynamics.

3.1.2 Inflow Modeling

Inflow is modeled based on the dynamic inflow model of Peters and HaQuang [11]. This is a nonlinear model, intended to be valid over a range of flight regimes, and therefore suitable for simulations of end-to-end missions. Inflow is represented as a uniform component plus a linear gradient over the rotor disk. The magnitudes depend on the generated thrust and aerodynamic moments, as well as the vertical and horizontal advance ratios. We use one model per rotor, but simulate interference by increasing the vertical advance ratio used in each model by a fraction of the uniform inflow component of the other rotor. Mars Helicopter experimental results to date indicate that a one-way coupling, with the lower rotor seeing the entire uniform component of the upper rotor, is a reasonable approximation. To account for ground effect, the uniform inflow component is restricted as a function of the distance above the terrain [see 6, Ch. 4.8].

Inflow modeling is known to be challenging; models of this type are semi-empirical and have been developed for large-scale, single-rotor helicopters on Earth. Thus, significant inaccuracies are expected when applying the same models to small-scale co-axial helicopters in Mars atmosphere. As described in Section 8, modifications must be implemented to account for effects observed in experiments.

3.2 Trim and Linearization

For control analysis and design, it is desirable to obtain linear time-invariant (LTI) models of the flight dynamics, as this enables the use of a wide variety of frequency-domain design and analysis tools. For helicopters, this is complicated by the periodic nature of the dynamics. Equilibrium in steady-state flight is characterized by a periodic trajectory, and linearizations along the equilibrium trajectory can be highly time-varying.

Similar to CAMRAD II, HeliCAT can be used to compute the periodic equilibrium trajectory for a given trim condition, and to output linearized models at a finite set of uniformly spaced points along the trajectory. A simple way to obtain an LTI model is to average the resulting periodic model; however, this method yields an inaccurate response for the Mars Helicopter model, due to the time-varying coupling between the rotor and fuselage with two-bladed rotors.

We instead post-process periodic linear time-variant models generated by HeliCAT using a method similar to Lopez and Prasad [9]. The method extends the vehicle state by in-

© 2017. All rights reserved.

cluding the coefficients of a truncated harmonic expansion:

$$x = x_0 + \sum_{i=1}^{n} (x_{ic} \cos(i\Omega t) + x_{is} \sin(i\Omega t)), \tag{1}$$

where Ω is the rotor angular rate. The periodic system dynamics obtained from the linearized models can be described by truncated harmonic expansions of the system matrices:

$$\begin{aligned} \dot{x} = &\left(A_0 + \sum_{i=1}^{n} (A_{ic} \cos(i\Omega t) + A_{is} \sin(i\Omega t)) \right) x \\ &+ \left(B_0 + \sum_{i=1}^{n} (B_{ic} \cos(i\Omega t) + B_{is} \sin(i\Omega t)) \right) u. \end{aligned} \tag{2}$$

We insert (1) into (2) and reduce products of frequencies to single frequencies through standard trigonometric identities, discarding frequencies above $n\Omega$. We extract into separate equations those terms that depend on each linearly independent harmonic, resulting in equations on the form

$$\dot{x}_0 - A_{00} x_0 + \sum_{k=1}^{n} (A_{0kc} x_{kc} + A_{0ks} x_{ks}) + B_0 u = 0,$$

$$\left(\dot{x}_{ic} - A_{ic0} x_0 + \sum_{k=1}^{n} (A_{ickc} x_{kc} + A_{icks} x_{ks}) + B_{ic} u \right) \mathrm{c}(i\Omega t) = 0,$$

$$\left(\dot{x}_{is} - A_{is0} x_0 + \sum_{k=1}^{n} (A_{iskc} x_{kc} + A_{isks} x_{ks}) + B_{is} u \right) \mathrm{s}(i\Omega t) = 0.$$

Discarding the harmonic multiplier and combining yields a high-order LTI system.

The output from the system is treated similarly, by decomposing the periodic system output as

$$y = \left(C_0 + \sum_{i=1}^{n} (C_{ic} \cos(i\Omega t) + C_{is} \sin(i\Omega t)) \right) x, \tag{3}$$

inserting (1), and extracting the resulting constant term from the right-hand side.

Empirically, an expansion up to $n = 4$ is necessary and sufficient for representing the Mars Helicopter frequency response with good accuracy.

4 Flap Dynamics

The flight dynamics of a helicopter are highly influenced by the dynamics of blade flapping. For a helicopter on Mars, the blade flapping dynamics diverges in important ways from that of Earth helicopters, due to to the low density of the atmosphere.

4.1 Fundamentals of Blade Flapping

When studying how blade flapping is affected by the low density of the Martian atmosphere, it is useful to start with the simplest-possible model of the blade, as a rod rotating about a flap hinge with a spring, as shown in Figure 6. Restoring moments about the flap hinge are present due to a combination of centrifugal stiffening and moments from the spring, and damping is present due to aerodynamic forces. The blade therefore acts like a classical mass-spring-damper system.

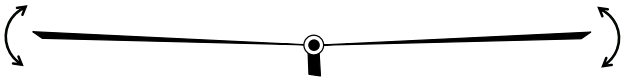

Figure 6: Illustration of blade flapping modeled by a central hinge with a spring.

When cyclic pitch is applied to a helicopter blade, a periodic change in lift is produced at the rotor frequency, with maximum lift on one side of the rotor disk, and minimum lift on the opposite side. A mass-spring-damper subjected to a periodic force will respond by settling into a periodic motion at the same frequency, but with a different phase than the input. Therefore, when cyclic control is applied to a helicopter rotor, it will settle into a periodic flapping motion that reaches its maximum at some point later than the maximum cyclic pitch. The flapping of the blade results in roll and pitch moments that are in general a combination of two effects: a tilt of the thrust vector, which results in moments proportional to the height of the rotor plane with respect to the center of gravity; and direct hub moments, due to resistance against flapping at the hub. For a more in-depth discussion, see Padfield [10].

The blue line in Figure 7 shows the magnitude and phase response of the blade flap angle in response to cyclic input for a *centrally hinged* rotor with *no hinge stiffness*. For this type of rotor, the restoring forces are all due to centrifugal stiffening, which places the natural frequency of the mass-spring-damper system exactly at the rotor frequency. As a result, the peak of the blade flapping, and the moments due to blade flapping, occur 90° after the peak cyclic pitch input. If the hinge is offset from the center, or it has additional hinge stiffness, the natural frequency will increase, and the phase lag between cyclic pitch input and blade flapping output will be reduced, in some cases to as little as 30–40° [see 5].

4.2 The Role of Aerodynamic Damping

The predominant source of damping of the flap motion is typically aerodynamic: as the blade flaps up or down, the angle-of-attack changes as a function of the flap rate; this produces a change in lift opposing the flap rate. For the simplified blade model with a central hinge, if the blade is additionally assumed to have a straight chord and a standard linear lift model is used, the nondimensional damping is given by

$$\zeta = \frac{\gamma}{16\omega_0}, \tag{4}$$

where ω_0 is the flap frequency nondimensionalized by the rotor frequency; and γ is the *blade Lock number*, a measure of the ratio of aerodynamic to inertial forces, given by

$$\gamma = \frac{\rho c C_{l\alpha} R^4}{I}. \tag{5}$$

Here, ρ is the air density, c is the chord length, $C_{l\alpha}$ is the lift curve slope of the blade airfoil, R is the rotor radius, and I is the blade inertia about the flap hinge. Blade Lock numbers for Earth helicopters are typically somewhere between 4 and 16. The response illustrated by the blue line in Figure 7 has a damping ratio of 25%, corresponding to a blade Lock number of 4 and $\omega_0 = 1$.

© 2017. All rights reserved.

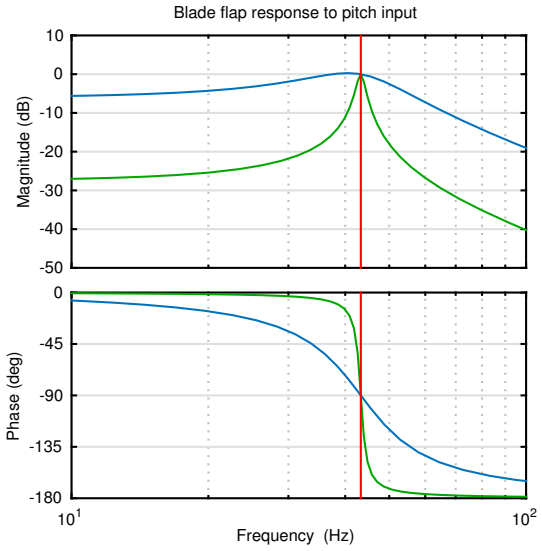

Figure 7: Magnitude and phase of blade flap angle response to pitch input, for a centrally hinged blade with no additional stiffness. Blue: typical Earth response with blade Lock number $\gamma = 4$. Green: hypothetical Mars response with blade Lock number $\gamma = 0.33$. The red line marks the rotor frequency.

Since the blade Lock number scales with density, we can expect it to be significantly reduced on Mars. Indeed, for the Mars Helicopter baseline design it falls roughly in the range between 0.3 and 0.6, depending on the density, which has a dramatic effect on damping of the flap dynamics. The green line in Figure 7 shows the response with the damping reduced to 2%, corresponding to a Lock number reduction to 0.33. It is clear that the phase angle is extremely sensitive around the natural frequency, and will quickly drop to near-zero if the rotor is stiffened to increase the natural frequency.

The azimuthal phase angle at steady-state is not fundamentally important for the controllability properties of the helicopter, as it is easily compensated for by adjusting the clocking of the cyclic inputs in order to produce roll and pitch moments. More concerning from the point-of-view of control is the *transient* flap response. A poorly damped mass-spring-damper takes longer to converge to steady-state; ultimately this manifests itself as poorly damped modes in the attitude response of the helicopter as a whole.

4.3 Effect of Flap Modes on the Helicopter Dynamics

The flap dynamics studied in the last section represents the motion of the blade when studied from the *rotating* frame. When controlling the helicopter, the interest is in the rotor dynamics in the *non-rotating* frame—that is, what is seen by an observer attached to the helicopter fuselage.

The moments in the nonrotating frame are a function both of the flap angle and the current azimuth of the blade. Thus, for a blade ringing at a nondimensional frequency ω_0, the moment about a fixed axis will be of the form

$$A\sin(\omega_0\psi)\sin(\psi+\varphi) = \frac{1}{2}A\cos((\omega_0-1)\psi-\varphi) - \frac{1}{2}A\cos((\omega_0+1)\psi+\varphi), \quad (6)$$

where ψ is the blade azimuth and φ is a phase angle. This illustrates the phenomenon that a single, poorly damped mode at frequency ω_0 gives rise to two modes in the non-rotating frame, at approximately $\omega_0 - 1$ and $\omega_0 + 1$, called the *regressing* and *advancing* modes.

A formal study of these modes, using coning and tip-path-plane coordinates, show that they inherit the low level of damping exhibited by the non-rotating flap mode. These ultimately show up as modes in the flight dynamics of the free-flying vehicle, at a shifted frequency due to freeing up the boundary condition of the fuselage. Figure 8 shows the magnitude of the transfer function from cosine cyclic (peaking at the rear of the rotor disk) to pitch angle, for for a particular version of the Mars helicopter dynamics that was studied at an early point. The regressing and advancing flap modes are clearly visible.

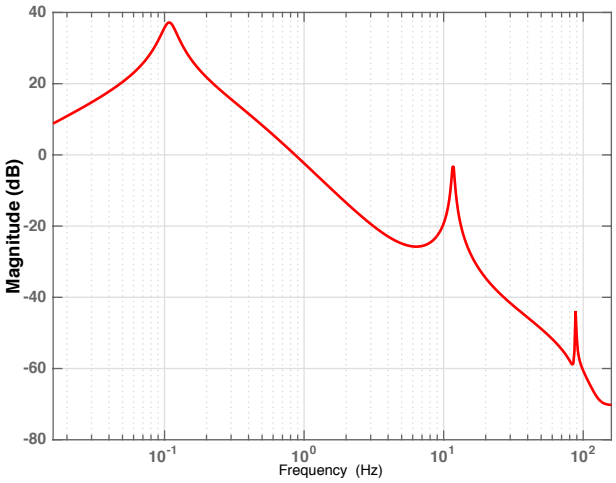

Figure 8: Magnitude of pitch angle frequency response to cosine cyclic input, for a particular version of the Mars Helicopter dynamics. The poorly damped regressing and advancing flap modes are clearly visible.

5 Consequences of Flap Dynamics for Control and Vehicle Design

Poorly damped modes like the ones shown in Figure 8 are problematic for control, due to the potential for destructive coupling with the control system itself. In response to vehicle motion at the resonant frequency, the feedback control system will apply an actuator input at the same frequency. Depending on the magnitude and phase, the response of the control system may amplify the resonance, leading to instability.

Although in some cases it is possible for a control system to "work around" resonances, using techniques of notch filtering or phase stabilization, the circumstances are not favorable for such a solution on the Mars Helicopter. This

© 2017. All rights reserved.

is in part due to the difficulty of accurately identifying the high-frequency dynamics; and in part because the high-frequency dynamics, once other sources of flexibility are included, become far more complicated than suggested by Figure 8.

A robust solution is is to ensure that the resonant frequencies are all well above the bandwidth of the control system, thereby preventing destructive control system interactions. This is achieved through the mechanical design of the helicopter by making the blades and hub for the Mars Helicopter unusually stiff, with a *rotating flap frequency of approximately* 80–90 *Hz*. Together with other stiffness requirements for the mast and landing gear, all resonant modes in the flight dynamics are then moved to high frequencies.

6 Sensitivity to Edgewise Flow

Helicopters typically react to edgewise flow by producing a pitch moment away from the wind. In a traditional helicopter, this is primarily due to the differences in lift on the advancing and retreating side of the rotor disk, which results in an effect similar to a cyclic control input peaking on the advancing side. When the moments generated due to periodic inputs have a significant phase lag, as is the case for Earth helicopters, the result is a pitch moment away from the wind. As explained in Section 4.2, the azimuthal phase lag in response to periodic inputs is very small for the Mars Helicopter; thus, lift differences on the advancing and retreating side will mostly result in a roll moments that are canceled out by an opposing moments from the other rotor.

However, another effect, due to inflow gradients across the rotor disk, comes into play, with much the same result. When the wake angle changes from the vertical due to the vehicle moving relative to the surrounding air, a longitudinal inflow gradient develops, resulting in more inflow at the rear of the disk and less at the front. This again results in a periodic change in lift, peaking at the front of the rotor disk. Due to the small azimuthal phase lag of the moments generated due to periodic inputs, the result is a pitch moment away from the wind. Rather than cancel each other, the moments from the two rotors act in concert.

6.1 Drawback of Stiff Rotor Design

The stiff rotor design exacerbates the vehicle's sensitivity to edgewise flow, through several different mechanisms:

- by reducing the azimuthal phase angle of moments in response to periodic inputs, the moments generated by the upper and lower rotor become more closely aligned, creating a larger additive moment
- the stiff rotor produces larger hub moments in response to edgewise flow, resulting in a faster transient response
- the stiff rotor reduces the *apparent inertia* of the coaxial helicopter—a phenomenon further discussed in Section 7.2—which also results in a faster transient response.

As will be discussed in Section 7.3, increased sensitivity to edgewise flow is undesirable both because of increased gust sensitivity and because it negatively affects the stability properties of the vehicle.

7 Low-Frequency Dynamics

A benefit of the stiff rotor design is that the linearized flight dynamics can be accurately described by a low-order model with only vehicle velocities, attitude, and angular rates as states, in the frequency range relevant for control. This model can be written as

$$\dot{x} = Ax + Bu, \tag{7}$$

where $x = [u; v; w; \varphi; \theta; \psi; p; q; r]$ contains the body-frame velocities relative to an inertial wind frame, the attitude Euler angles, and the body-frame angular rates; and $u = [\theta_{l0}; \theta_{lc}; \theta_{ls}; \theta_{u0}; \theta_{uc}; \theta_{us}]$ contains the lower collective, cosine cyclic, and sine cyclic, followed by the upper collective, cosine cyclic, and sine cyclic. We use the convention that the x axis points forward on the vehicle; the y axis points to the right; and the z axis points down. The A and B matrices are written in standard form as

$$A = \begin{bmatrix} X_u & X_v & X_w & 0 & -g\mathrm{c}\bar{\theta} & 0 & X_p & X_q - \bar{w} & X_r + \bar{v} \\ Y_u & Y_v & Y_w & g\mathrm{c}\bar{\varphi}\mathrm{c}\bar{\theta} & -g\mathrm{s}\bar{\varphi}\mathrm{s}\bar{\theta} & 0 & Y_p + \bar{w} & Y_q & Y_r - \bar{u} \\ Z_u & Z_v & Z_w & -g\mathrm{s}\bar{\varphi}\mathrm{c}\bar{\theta} & -g\mathrm{c}\bar{\varphi}\mathrm{s}\bar{\theta} & 0 & Z_p - \bar{v} & Z_q + \bar{u} & Z_r \\ 0 & 0 & 0 & 0 & 0 & 0 & 1 & \mathrm{s}\bar{\varphi}\mathrm{t}\bar{\theta} & \mathrm{c}\bar{\varphi}\mathrm{t}\bar{\theta} \\ 0 & 0 & 0 & 0 & 0 & 0 & 0 & \mathrm{c}\bar{\varphi} & -\mathrm{s}\bar{\varphi} \\ 0 & 0 & 0 & 0 & 0 & 0 & 0 & \mathrm{s}\bar{\varphi}/\mathrm{c}\bar{\theta} & \mathrm{c}\bar{\varphi}/\mathrm{c}\bar{\theta} \\ L_u & L_v & L_w & 0 & 0 & 0 & L_p & L_q & L_r \\ M_u & M_v & M_w & 0 & 0 & 0 & M_p & M_q & M_r \\ N_u & N_v & N_w & 0 & 0 & 0 & N_p & N_q & N_r \end{bmatrix}$$

and

$$B = \begin{bmatrix} X_{L0} & X_{LC} & X_{LS} & X_{U0} & X_{UC} & X_{US} \\ Y_{L0} & Y_{LC} & Y_{LS} & Y_{U0} & Y_{UC} & Y_{US} \\ Z_{L0} & Z_{LC} & Z_{LS} & Z_{U0} & Z_{UC} & Z_{US} \\ 0 & 0 & 0 & 0 & 0 & 0 \\ 0 & 0 & 0 & 0 & 0 & 0 \\ 0 & 0 & 0 & 0 & 0 & 0 \\ L_{L0} & L_{LC} & L_{LS} & L_{U0} & L_{UC} & L_{US} \\ M_{L0} & M_{LC} & M_{LS} & M_{U0} & M_{UC} & M_{US} \\ N_{L0} & N_{LC} & N_{LS} & N_{U0} & N_{UC} & N_{US} \end{bmatrix}.$$

We have denoted by $[\bar{u}; \bar{v}; \bar{w}]$ the body-frame trim velocities; by $\bar{\varphi}$ and $\bar{\theta}$ the trim roll and pitch attitudes; and by g the acceleration of gravity. The remaining components of A and B are stability and control derivatives that capture sensitivities of the vehicle motion to the states and control inputs.

7.1 Model Reduction

Via a custom optimization process, low-order models on the form (7) can be generated to match the frequency response of a full-order model derived from the process outlined in Section 3.2. The process can be summarized as follows: We set up the full-order linear system so that its inputs match those of the reduced-order system, and its outputs match the states of the reduced-order system. The full-order system with these inputs and outputs can be written in transfer function form as

$$x(s) = H(s)u(s). \tag{8}$$

We select a set of evaluation frequencies ω_i, $i = 1, \ldots, n$, logarithmically spaced over the frequency range of interest.

© 2017. All rights reserved.

For each frequency ω_i, we compute the steady-state frequency response $H_i := H(j\omega_i)$.

For each input component k, and for each state component ℓ, we know that the input $u_k = \sin(\omega_i t)$ yields the steady-state response $x_\ell = |h_{i\ell k}|\sin(\omega_i t + \angle h_{i\ell k})$, where $h_{i\ell k}$ is element (ℓ, k) of H_i. We furthermore know that the steady-state response of the time derivative is $\dot{x}_\ell = \omega_i |h_{i\ell k}|\cos(\omega_i t + \angle h_{i\ell k})$. We now want to find A and B such that the same is true for the reduced-order system (7). This would require that the following hold:

$$\omega_i \begin{bmatrix} |h_{i11}|\,\mathrm{c}(\omega_i t + \angle h_{i11}) & \cdots & |h_{i16}|\,\mathrm{c}(\omega_i t + \angle h_{i16}) \\ \vdots & \ddots & \vdots \\ |h_{i91}|\,\mathrm{c}(\omega_i t + \angle h_{i91}) & \cdots & |h_{i96}|\,\mathrm{c}(\omega_i t + \angle h_{i96}) \end{bmatrix} = A \begin{bmatrix} |h_{i11}|\,\mathrm{s}(\omega_i t + \angle h_{i11}) & \cdots & |h_{i16}|\,\mathrm{s}(\omega_i t + \angle h_{i16}) \\ \vdots & \ddots & \vdots \\ |h_{i91}|\,\mathrm{s}(\omega_i t + \angle h_{i91}) & \cdots & |h_{i96}|\,\mathrm{s}(\omega_i t + \angle h_{i96}) \end{bmatrix} + B\,\mathrm{s}(\omega_i t). \tag{9}$$

The above set of $9 \cdot 6 = 54$, equations, which is continuous in t, can be reduced to two sets of equations independent of t by evaluating at $t = 0$ and $t = \pi/(2\omega_i)$. This involves no loss of information, since (9) can be written for any other t as a linear combination of those two sets of equations.

By combining the two sets of equations extracted for each frequency ω_i, we have obtained a total of $54 \cdot 2 \cdot n = 108n$ linear equations with real coefficients. The unknowns are those elements of A and B that are not known *a priori*. We now estimate the unknowns by performing a least-squares fit, thus yielding the A and B matrices for the reduced-order model.

Figure 9 shows the magnitude of the full-order and reduced-order frequency response of the transfer function from cosine cyclic input to the helicopter pitch angle, for an up-to-date model of the Mars Helicopter in hover. It is notable that the low-order model matches the high-order model well up to frequencies of approximately 10 Hz. This is adequate for relying on the low-order formulation for control analysis and design.

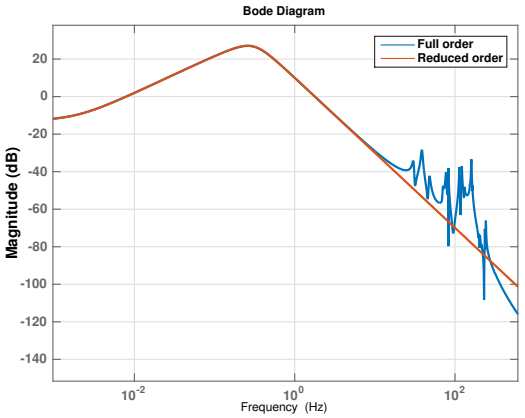

Figure 9: Comparison of the full-order and reduced-order linear models, for an up-to-date model of the Mars Helicopter. The complicated dynamics at high frequency is a result of poorly damped rotor dynamics, combined with flexibility of the mast and the landing gear.

7.2 Apparent Inertia

A rigid body with no angular momentum, when subjected to a torque of magnitude τ about a principal axis, responds with an angular acceleration of magnitude τ/I about the same axis, where I is the moment of inertia about the relevant axis. For a coaxial helicopter with stiff, counter-rotating rotors, it would seem reasonable to expect a low-frequency behavior consistent with that of a rigid body, with an inertia corresponding to the *average* inertia of the system helicopter.

To investigate this hypothesis, consider a simple example system consisting of a rigid central body attached to two perfectly stiff, 2-bladed counter-rotating rotors. The central body has its center of mass at the origin and has a diagonal inertia matrix of magnitude $I_c = 0.02$ kg·m^2 in all three axes. The rotors are both centered at the origin and rotate about the z axis at a rate of $\Omega = 272$ rad/s, and each blade has the inertia of a simple rod—zero about the symmetry axis and $I_b = 0.002$ kg·m^2 in the other two axes. The average inertia over one rotation is therefore $I_{av} = I_c + 2I_b = 0.024$ kg·m^2. We apply a constant torque to this body of magnitude $\tau_x = 0.1$ Nm about the x axis, as the only external force in the system. Figure 10 shows the simulated angular velocities of the central body in response to this torque. When the high-frequency vibrations are averaged out, the system exhibits a linear increase in x axis angular velocity at a rate of 4.2 rad/s^2, which matches the formula $\tau_x/I_{av} = 4.2$ rad/s^2. Thus, we conclude that the low-frequency response is indeed as hypothesized in the previous paragraph.

Next consider the same system, but with the rotors free to flap about a central hinge. The hinge is stiffened with a spring with a spring rate of 500 Nm/rad, which yields a rotating flap frequency of 91 Hz when centrifugal stiffening is accounted for. Figure 11 shows the simulated response. The angular acceleration is still about the x axis, but the magnitude is reduced to 3.5 rad/s^2—that is, the system still responds similar to a rigid body, but it responds as though a smaller torque of approximately 0.08 Nm is being applied.

To understand this phenomenon, we need to locate the "missing" 0.02 Nm torque that is being applied to the system, but which does not manifest itself in the gross vehicle motion. To this end, consider Figure 12, where the tip-path-plane of each rotor is plotted for the same simulation. The tip-path-planes exhibit a linearly growing tilt about the y axis in response to the x axis input, in opposite directions. The rate of change has a magnitude of approximately $\dot{\beta} = 0.01$ rad/s when high-frequency vibrations are averaged out. Using standard equations for gyroscope motion, we find that the torque required to effect this linear growth is $\dot{\beta}H = 2\dot{\beta}\Omega I_b \approx 0.01$ Nm for each rotor, where H denotes the magnitude of the angular momentum for each rotor. This accounts for the missing torque.

The phenomenon observed in this example is due to gyroscopic effect on the two rotors, which causes the rotors to realign themselves with opposing tilts about the y axis in response to a torque about the x axis. While the rigid rotor head prevents any reorientation from happening, the flexible rotor head allows for a limited amount of reorientation—even

© 2017. All rights reserved.

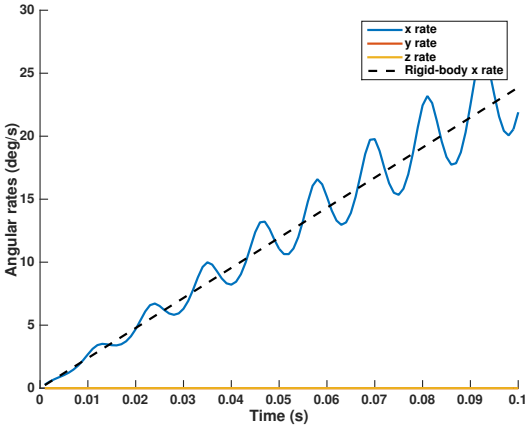

Figure 10: Angular velocity response to constant torque, for the simplified example system with a perfectly rigid rotor. The dashed black line shows the response expected from a perfect rigid body with an inertia corresponding to the average inertia of the rotating system.

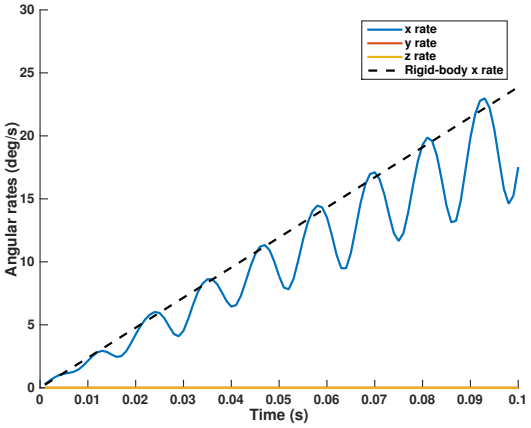

Figure 11: Angular velocity response to constant torque, for the simplified example system with a flapping rotor. The dashed black line shows the response expected from a perfect rigid body with an inertia corresponding to the average inertia of the rotating system.

for very stiff rotors—thereby "absorbing" some of the torque applied to the system and giving it a larger apparent inertia.

7.2.1 A Formula for Apparent Inertia

By modeling the system as two counter-rotating gyroscopes on a central body, and calculating the DC gain from a torque input to the angular accelerations, the following formula can be derived for the apparent inertia:

$$I_{apparent} = I_{actual} + \frac{2H^2}{k}, \tag{10}$$

where I_{actual} is the total x/y inertia of the system, and k is the torsional spring constant between each gyroscope and the central body.

A very simple argument can be formulated as follows: for a steady-state angular rate ω_x about the x axis, the total

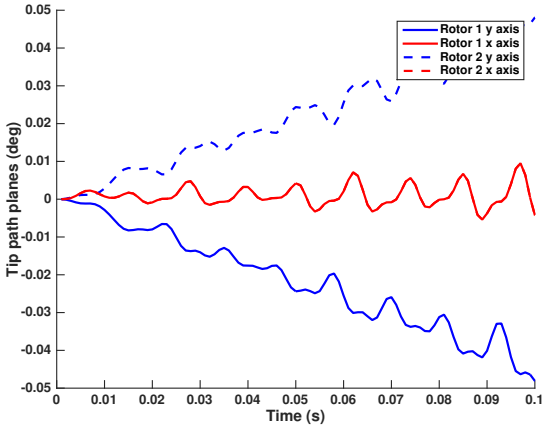

Figure 12: Tip-path-plane response to constant torque, for the simplified example system with a flapping rotor.

angular momentum is

$$H_{total} = I_{actual} \cdot \omega_x + H_1\beta_{y1} + H_2\beta_{y2}, \tag{11}$$

where H_1 and H_2 are the angular momentums of the gyroscopes, and β_{y1} and β_{y2} are the gyroscope tilts about the central body's y axis. For each gyroscope to maintain a steady-state rate about the x axis, it must be acted upon by a y axis torque $-H_{\{1,2\}}\omega_x$, which must necessarily be equal to the spring torque $-k\beta_{y\{1,2\}}$, since this is the only external torque on the gyroscope. Combining these expressions, we have

$$\beta_{y\{1,2\}} = \frac{H_{\{1,2\}}\omega_x}{k}. \tag{12}$$

Inserting into (11), we obtain

$$H_{total} = I_{actual} \cdot \omega_x + \frac{2H^2\omega_x}{k}. \tag{13}$$

If we now compute $I_{apparent} = H_{total}/\omega_x$, we obtain (10).

The formula (10) can be used to approximate the effect for a helicopter with discrete blades, by replacing I_{actual} with the average inertia, and k with the spring constant of each blade, multiplied by $N/2$, where N is the number of blades on each rotor. Applied to the example in the last section, we obtain $I_{apparent} = 0.029$ kg·m^2, which is consistent with the observed response.

7.3 Open-Loop Stability

Unlike most vehicles, helicopters are almost always unstable in open loop, with poles in the open right-half complex plane. This is no different for helicopters on Mars, as indicated in Figure 13, which shows the open-loop poles of the hover dynamics for an up-to-date model of the Mars Helicopter. The dynamics exhibit four stable subsidence modes in the open left-half complex plane; one marginally stable mode at the origin; and four unstable modes in the open right-half complex plane. The mode at the origin is due to the yaw angle being included in the state vector. The modes in the right-half complex plane are longitudinal and lateral *phugoid* modes that result from a coupling between the attitude and horizontal speed states.

© 2017. All rights reserved.

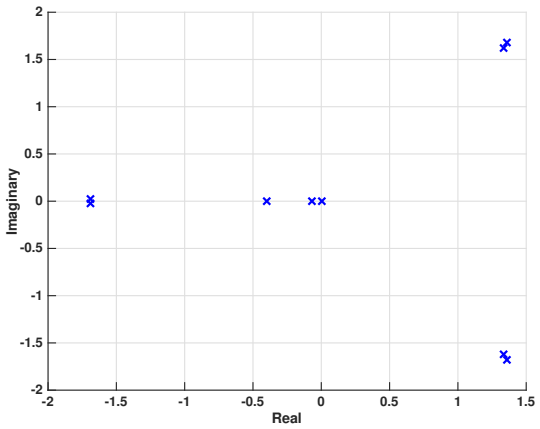

Figure 13: Poles of the low-frequency dynamics of the demonstration vehicle.

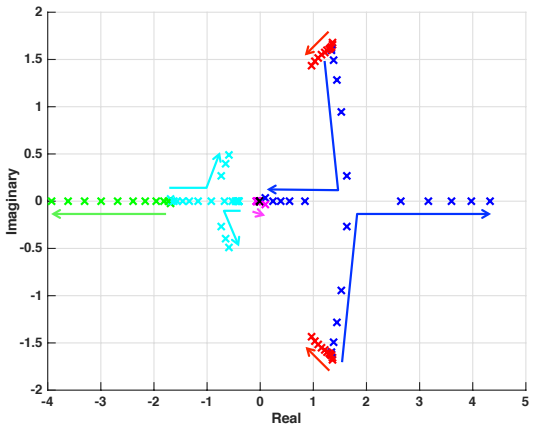

Figure 14: Root loci of the helicopter dynamics, transitioning from hover to forward flight at 10 m/s airspeed. The blue and red arrows indicate the evolution of the longitudinal and lateral phugoids, respectively. The pole moving further out into the right-half complex plane corresponds to the pitch-heave instability that develops in forward flight.

To see what drives these modes, consider the longitudinal dynamics only, restricted to the pitch angle, pitch rate, and longitudinal velocity. Assume furthermore that X_u, X_q, and M_q are zero, which is close to the truth for the Mars Helicopter. At hover with zero trim angles, the resulting system matrix is given by

$$A_l = \begin{bmatrix} 0 & -g & 0 \\ 0 & 0 & 1 \\ M_u & 0 & 0 \end{bmatrix}.$$

The stability derivative M_u represents the sensitivity of the helicopter's pitch rate to longitudinal speed; or equivalently, the sensitivity to a gust from the front. It is positive, because increased longitudinal velocity results in a nose-up moment.

The characteristic equation of A_l is given by $\lambda^3 + M_u g = 0$, with solutions $\lambda_1 = -\sqrt[3]{M_u g}$, $\lambda_{\{2,3\}} = \frac{1}{2}(1 \pm \sqrt{3}j)\sqrt[3]{M_u g}$. It is clear that the frequency of the unstable poles increases with both M_u and g. We can therefore make the following observations:

- As discussed in Section 6, the high rotor stiffness results in increased sensitivity to edgewise flow, which manifests itself as an increase in the magnitude of M_u. This results in an increase in the frequency of the unstable modes.
- The unstable modes for a helicopter operating in Mars gravity will have reduced frequency compared to Earth.

The unstable nature of the open-loop dynamics is highly significant in the context of control design, as it imposes fundamental limitations on the achievable stability margins, which become more severe as the frequency of the instability increases [see 14].

7.4 Forward Flight

The dynamics of the helicopter changes as it moves from hover to forward flight. In particular, the helicopter exhibits the classical trait of developing a pitch-heave instability, as seen from the root-loci in Figure 14.

The pitch-heave instability is driven by the emergence of a positive M_w stability derivative. Consider forward flight at a positive trim longitudinal velocity $\bar{u}$. In response to a positive perturbation in w (i.e., a downward movement), the helicopter pitches nose-up due to the positive M_w, resulting in a positive pitch rate. Due to the kinematic coupling between pitch rate and vertical velocity, captured by the element $Z_q + \bar{u}$ in the A matrix, w increases further, thus making the effect self-amplifying.

For the Mars Helicopter flight dynamics model, the positive M_w in forward flight is primarily driven by inflow effects. In trim forward flight, the wake angle is deflected from the vertical, resulting in an inflow gradient whose effect is counteracted by the cyclic trim settings. A positive perturbation in w reduces the net inflow through the rotor, thus increasing the wake angle. This results in an increased inflow gradient, which gives rise to a nose-up pitch moment.

8 System Identification

The identification of the helicopter bare-airframe system dynamics is crucial to the design of a stable flight control system. Despite the extensive modeling and simulation effort, testing is needed to fully understand the vehicle behavior, especially given the lack of prior work on helicopter dynamics in Martian conditions. A system identification program has therefore been developed to identify the actual dynamics of the helicopter.

A unique challenge of flight dynamics testing of a Mars Helicopter is the difficulty of replicating the Martian conditions; in particular, low density conditions cannot be combined with emulation of Martian gravity in a practical way. While helicopter mass can be offloaded to match the weight on Mars, this cannot be achieved without changing the center of mass and inertia of the vehicle. Further limitations include the availability of a test facility with sufficient space for end-to-end testing, and the complication of replicating the full range of environmental disturbances (wind and gusts). Given these limitations, a "piecewise" system identification

© 2017. All rights reserved.

approach is adopted, in which individual parameters relevant to the bare-airframe dynamics (i.e., control derivatives, speed stability derivatives, attitude damping derivatives, inertias, etc.) are targeted via specific tests designed to be performed in the confined space of a vacuum chamber.

8.1 System Identification for the Demonstration Vehicle

The system identification process for the demonstration vehicle focused on the hover condition only, using a process based on three test configurations:

1. *Locked-down configuration*: the helicopter was mounted on a force-torque sensor.

2. *Swinging-arm configuration*: the helicopter was mounted on a force-torque sensor at the end of a swinging arm.

3. *Gimbal configuration*: the helicopter was mounted on a gimbal with roll and pitch degrees of freedom.

In the locked-down and gimbal configurations, the helicopter controls were exercised with different inputs. On the swinging arm, the arm motion was prescribed to emulate a desired translational motion, while approximately fixing the rotational motion (the swinging motion inherently imparts some angular motion).

The first tests were conducted with the helicopter locked down. In this configuration, the rotational degrees of freedom of the vehicle were constrained, and the controls were subjected to:

- high-frequency sweeps: designed to verify available actuator control bandwidth and that undesirable high-frequency rotor modes are not within the frequency range desired for control; and

- moderate-duration doublets: designed to identify the quasi-steady vehicle control (force and moment) derivatives.

Force and torque reactions on the force-torque sensor were measured and used for estimation of the derivatives with respect to the control inputs. The apparent roll and pitch inertia of the vehicle was unknown at this stage; thus the absolute magnitude of the control derivatives in roll and pitch could not yet be determined.

On the swinging arm, the vehicle was swung back and forth to generate edgewise flow over the rotor; and to generate flow perturbations through the rotor by changing the mounting orientation on the arm. The resulting forces and moments were measured to determine the speed stability derivatives. As with the control derivatives, roll and pitch moment speed derivatives could not yet be positively identified because of the unknown apparent inertia.

Finally, control input frequency sweeps were applied to the helicopter on the gimbal, which allowed the excitation of the roll and pitch rates required for the system identification of the bare-airframe roll and pitch dynamics. Among the system parameters identified was the apparent inertia in roll and pitch, which provided the missing piece of information necessary to determine the control and speed stability derivatives in roll and pitch.

In order to maintain stability on the gimbal, a low-bandwidth controller was implemented to maintain attitude while minimizing control input cross-coupling. A tether with a pre-loaded spring was used to restrain the vehicle during spin-up and spin-down, and to partially restrain the vehicle during some of the tests. This tether had the effect of introducing a restoring moment as a function of the attitude, which had to be accounted for in the identification process.

Different system identification methods, including the time-domain examination of the steady-state response to doublet inputs, and frequency-domain methods for the analysis of the system response to sinusoidal frequency sweeps were employed. The latter frequency-response analysis made extensive use of the methods implemented in the software package *Comprehensive Identification from Frequency Responses (CIFER)*, developed at Ames Research Center [see 16].

8.1.1 System model

The model to be identified was defined by a slightly modified form of (7) that is considered valid for the hover condition:

$$M\dot{x} = Fx + Gu + r_G, \tag{14}$$

where

$$M = \begin{bmatrix} m & 0 & 0 & 0 & 0 & 0 & 0 & 0 & 0 \\ 0 & m & 0 & 0 & 0 & 0 & 0 & 0 & 0 \\ 0 & 0 & m & 0 & 0 & 0 & 0 & 0 & 0 \\ 0 & 0 & 0 & 1 & 0 & 0 & 0 & 0 & 0 \\ 0 & 0 & 0 & 0 & 1 & 0 & 0 & 0 & 0 \\ 0 & 0 & 0 & 0 & 0 & 1 & 0 & 0 & 0 \\ 0 & 0 & 0 & 0 & 0 & 0 & I_{xx} & I_{xy} & 0 \\ 0 & 0 & 0 & 0 & 0 & 0 & I_{yx} & I_{yy} & 0 \\ 0 & 0 & 0 & 0 & 0 & 0 & 0 & 0 & I_{zz} \end{bmatrix} \tag{15}$$

is the "mass matrix" of the helicopter. The total vehicle mass m and the yaw inertia I_{zz} are known parameters and can be treated as such in the system identification problem. However, because of the apparent inertia effect, the roll and pitch inertias were treated as unknown parameters to be identified. The remaining matrices in (14) are

$$F = \begin{bmatrix} X_u & X_v & 0 & 0 & -mg & 0 & X_p & X_q & 0 \\ Y_u & Y_v & 0 & mg & 0 & 0 & Y_p & Y_q & 0 \\ 0 & 0 & Z_w & 0 & 0 & 0 & 0 & 0 & Z_r \\ 0 & 0 & 0 & 0 & 0 & 0 & 1 & 0 & 0 \\ 0 & 0 & 0 & 0 & 0 & 0 & 0 & 1 & 0 \\ 0 & 0 & 0 & 0 & 0 & 0 & 0 & 0 & 1 \\ L_u & L_v & 0 & 0 & 0 & 0 & L_p & L_q & 0 \\ M_u & M_v & 0 & 0 & 0 & 0 & M_p & M_q & 0 \\ 0 & 0 & N_w & 0 & 0 & 0 & 0 & 0 & N_r \end{bmatrix}$$

and

$$G = \begin{bmatrix} 0 & X_{LC} & X_{LS} & 0 \\ 0 & Y_{LC} & Y_{LS} & 0 \\ Z_{S0} & 0 & 0 & Z_{A0} \\ 0 & 0 & 0 & 0 \\ 0 & 0 & 0 & 0 \\ 0 & 0 & 0 & 0 \\ 0 & L_{LC} & L_{LS} & 0 \\ 0 & M_{LC} & M_{LS} & 0 \\ N_{S0} & 0 & 0 & N_{A0} \end{bmatrix}.$$

© 2017. All rights reserved.

The corresponding state vector is arranged as $x = [u; v; w; \varphi; \theta; \psi; p; q; r]$. The input vector is defined as $u = [\theta_{s0}; \theta_{lc}; \theta_{ls}; \theta_{a0}]$, where θ_{s0} and θ_{a0} are the symmetric and anti-symmetric collective components:

$$\theta_{s0} = \frac{1}{2}(\theta_{l0} + \theta_{u0}), \quad \theta_{a0} = \frac{1}{2}(\theta_{l0} - \theta_{u0}). \tag{16}$$

Swashplate servo-actuator dynamics were assumed to be of a second-order nature, with a time delay:

$$\frac{\theta_k(s)}{\theta_{k_{cmd}}(s)} = \frac{\omega_k^2 e^{-\tau_k s}}{s^2 + 2\zeta_k \omega_k s + \omega_k^2}.$$

It was ascertained early on that it would not be possible to experimentally measure the actual value of the bare-airframe control inputs θ_{l0}, θ_{lc}, θ_{ls}, and θ_{a0}. Therefore, the inputs of the parametric model structure were actually defined in terms of the command input signals $\theta_{s0_{cmd}}$, $\theta_{lc_{cmd}}$, $\theta_{ls_{cmd}}$, and $\theta_{a0_{cmd}}$. In doing so, the servo-actuator dynamic properties (ω_k, ζ_k and τ_k) also become parameters of the system that need to be identified. Apart from the time delays, actuators were assumed to be identical, capturing the global combined effect of the individual actuators. Specifying different time delays allows for the problem to account for unmodeled high-frequency dynamics in each axis which may appear as an effective additional delay.

The term r_G on the right-hand side of (14) generically represents the effect of the external forces and moments acting on the model, such as the gimbal or force-torque sensor reactions.

8.1.2 System Identification Findings

The system identification approach was successful in determining the key parameters of the system. Many of the smaller parameters could not be reliably identified due to noise and aerodynamic disturbances; however, this was expected and is of little consequence because of their limited impact on the dynamics.

The identified parameters matched analytical model predictions with reasonable accuracy, but notable differences were found in certain areas, as discussed in the following paragraphs. Among these, only the first two have a significant impact on the stability and controllability properties of the system.

Rotor damping Contrary to typical helicopter behavior, rotor aerodynamic damping of the roll and pitch rates was found to be negative, meaning that roll and pitch rates are self-amplifying rather than decaying. This was reflected in the positive values of the identified on-axis roll and pitch damping derivatives M_q and L_p (values on the order of 0.4–0.45 rad/s). The likely cause is a dependence of the inflow gradients on the roll and pitch rates of the rotor disk, which is not included in the inflow model of Peters and HaQuang [11] but can be found elsewhere [e.g., 6, Ch. 11.3] and is typically captured by a parameter denoted by K_R. The inclusion of this effect increases the inflow over the rear side of the rotor disk for a nose-up pitch rate, which in turn creates a larger positive moment. This effect on the inflow gradient typically changes the off-axis response to control inputs, but due to the peculiarities of the Mars Helicopter flap dynamics (see Section 4), it instead has the effect of removing the roll and pitch damping. A value of $K_R = 2.9$ was needed to replicate the behavior in simulation models.

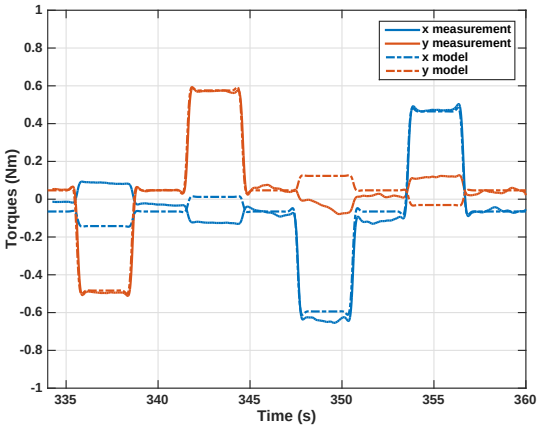

Figure 15: Comparison of measured and *a priori* modeled roll and pitch torques in response to steps in the cyclic channels. Three-second steps of 5° in cosine cyclic (positive, then negative) are followed by similar steps in sine cyclic. Note that cosine cyclic peaks at the rear of the rotor disk (along negative x), and sine cyclic peaks on the right-hand-side of the rotor disk (along positive y). The data has been filtered with a 2-Hz lowpass filter and a constant offset has been removed for better comparison. The less-clean data in the second-half of the plot are due to air recirculation in the chamber, which tended to manifest itself after 10–15 s in each test.

Sensitivity to edgewise flow Data from the swinging-arm test, although noisy, indicates that the on-axis moments generated due to edgewise flow, as captured by the stability derivatives M_u and L_v, were significantly larger than expected. This is most likely due to the development of a larger inflow gradient than predicted by the inflow model of Peters and HaQuang [11]. By adding a tuning parameter to amplify the sensitivity of the inflow gradient to edgewise flow by a factor of approximately 2.5, the results can be reproduced in simulation. The increased sensitivity has a negative effect on the open-loop stability properties of the system (see Section 7.3).

Unmodeled dynamics in thrust response Slow (0.4–0.5 Hz) unmodeled dynamics, resembling a highly damped pole-zero pair, were uncovered in the thrust response to symmetric collective. The mode was sufficiently below the control crossover frequencies and did not exhibit any persistent drop-off in phase, and as such was not considered problematic for control design. The source of this unmodeled dynamics is likely a coupling with the rotor RPM controller, rather than an aerodynamic effect.

Phasing of roll/pitch moments *A priori* modeling indicated that moments in response to cyclic would *lead* the applied cyclic by approximately 8°, due to unsteady aerodynamic effects from the angular velocity of the blade. Test results instead indicated a lag of approximately 11° (see Figure 15). The lag cannot be explained by any reasonable change in the stiffness of the rotor; it is instead hypothesized

© 2017. All rights reserved.

that it may be due to a small lag in the buildup of aerodynamic lift forces in response rapid angle-of-attack changes. The effect can be replicated in simulation models by the addition of a first-order aerodynamic lag with a time constant of approximately 1.7 ms.

Thrust and yaw torque response to collective Moderate discrepancies in the steady-state thrust and torque responses to symmetric and anti-symmetric collective step inputs were found to be consistent with a momentum theory under-prediction of the uniform inflow component by approximately 20%.

Apparent inertia The apparent inertia, as measured by the relationship between the roll and pitch control derivatives and the moments measured on the force-torque sensor, was found to be larger than predicted based on simulation, adding approximately 60% to the rigid-rotor case as opposed to a predicted increase of approximately 50%. Although the effect can be reproduced by lowering the rotor stiffness, measurements of the vehicle stiffness are not consistent with this being the true underlying cause. We instead hypothesize that the increased apparent inertia is related to the distributed and high-order nature of the rotor flexing, which is not captured by the single-hinge model used to predict the effect *a priori*.

9 Free-Flight Demonstration

Despite certain challenges related to the flight dynamics of the proposed Mars Helicopter, it is possible to design controllers with good stability margins and adequate performance within the intended flight envelope, provided latencies are kept small and the actuators have sufficiently high bandwidth. Such a design was carried out for the demonstration vehicle described in Section 2.1, and the vehicle was flown successfully in JPL's 25-ft Space Simulator, in CO_2 at a density of 0.0175 kg/m^3. The flight was fully autonomous, consisting of takeoff, climb to an altitude of 2 m at a rate of 1 m/s, hover for 30 s, descent at 0.5 m/s, and landing. A picture of the flying vehicle can be seen in Figure 16. The position of the vehicle during the demonstration flight is shown in Figure 17. During flight, the vehicle created its own gusty weather within the chamber, which accounts for the variation in position during the hover portion. The control design will be described in an upcoming paper [4].

10 Concluding Remarks

As discussed in this paper, analysis of helicopter flight dynamics for Mars has revealed a number of significant differences with typical Earth helicopter dynamics. Some of these pose challenges for closed-loop control. Nonetheless, with the successful completion of a system identification and free-flight demonstration campaign, the feasibility of controlled helicopter flight in Martian atmosphere has been established. This marks a significant step toward the ultimate goal of flying on Mars.

At the current point in time, development is progressing on a flight-ready Mars vehicle, and tests are being prepared for further system identification and flight testing, as well as

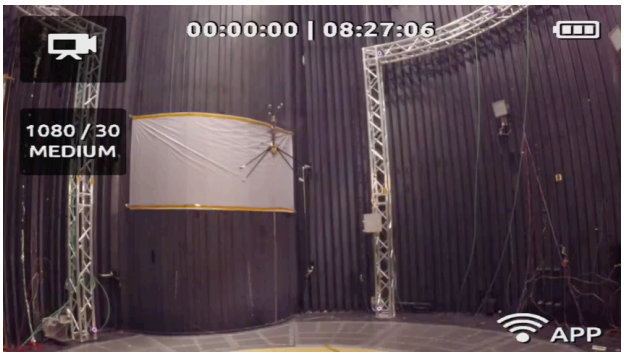

Figure 16: The Mars Helicopter demonstration vehicle in hover, inside JPL's 25-ft Space Simulator.

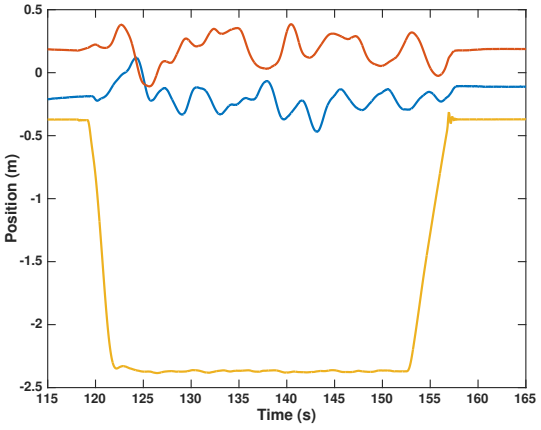

Figure 17: Estimated vehicle position (center of mass relative to ground frame, represented in ground frame) during free-flight demonstration. Recall that positive *z* axis is down.

environmental testing (radiation, thermal, vibration, etc.). A main point of interest in upcoming tests will be the identified vehicle behavior in forward flight, which has been modeled but not covered by actual tests to date. The helicopter dynamics in forward flight tends to exhibit faster instabilities and greater levels of cross-axis coupling. Analysis to date nevertheless shows that adequate stability margins and performance can be achieved within the desired flight envelope.

References

[1] E. W. Aiken, R. A. Ormiston, and L. A. Young. Future directions in rotorcraft technology at Ames research center. In *Proc. American Helicopter Society Annual Forum*, Virginia Beach, VA, 2000.

[2] J. Balaram and P. T. Tokumaru. Rotorcrafts for Mars exploration. In *Proc. International Planetary Probe Workshop*, Pasadena, CA, 2014. LPI Contribution No. 1795.

[3] A. Datta, B. Roget, D. Griffiths, G. Pugliese, J. Sitaraman, J. Bao, L. Liu, and O. Gamard. Design of the Martian autonomous rotary-wing vehicle. In *Proc. AHS*

© 2017. All rights reserved.

Specialist Meeting on Aerodynamics, Acoustics, and Test and Evaluation, San Francisco, CA, 2002.

[4] H. F. Grip, D. P. Scharf, C. Malpica, W. Johnson, M. Mandić, G. Singh, and L. Young. Guidance and control for a Mars helicopter. Submitted to AIAA Guidance, Navigation, and Control Conference, 2018.

[5] D. H. Halley. ABC helicopter stability, control, and vibration evaluation on the Princeton Dynamic Model Track. In *Proc. American Helicopter Society 29th Annual Forum*, Washington, DC, 1973.

[6] W. Johnson. *Rotorcraft Aeromechanics*. Cambridge University Press, 2013.

[7] I. Kroo and P. Kunz. Development of the Mesicopter: A miniature autonomous rotorcraft. In *Proc. American Helicopter Society Vertical Lift Aircraft Design Conf.*, San Francisco, CA, 2000.

[8] C. Lim and A. Jain. Dshell++: A component based, reusable space system simulation framework. In *Proc. Third IEEE International Conference on Space Mission Challenges for Information Technology*, Pasadena, CA, 2009.

[9] M. Lopez and J. V. R. Prasad. Linear time invariant approximations of linear time periodic systems. In *Proc. European Rotorcraft Forum*, Munich, Germany, 2015.

[10] G. D. Padfield. *Helicopter Flight Dynamics: The Theory and Application of Flying Qualitites and Simulation Modeling*. AIAA, 1996.

[11] D. A. Peters and N. HaQuang. Dynamic inflow for practical applications. *J. American Helicopter Society*, 33 (4):64–68, 1988.

[12] G. Savu and O. Trifu. Photovoltaic rotorcraft for Mars missions. In *Proc. Joint Propulsion Conf. and Exhibit*, San Diego, CA, 1995.

[13] H. Song and C. Underwood. A Mars VTOL aerobot – preliminary design, dynamics and control. In *Proc. IEEE Aerospace Conference*, 2007.

[14] G. Stein. Respect the unstable. *IEEE Control Systems Magazine*, 23(4):12–25, 2003.

[15] B. Thompson. Full throttle to Mars. Rotor & Wing, Phillips Business Information, LLC, Potomac, MD, 2001.

[16] M. B. Tischler and R. K. Remple. *Aircraft and Rotorcraft System Identification: Engineering Methods with Flight Test Examples*. AIAA, 2012.

[17] N. Tsuzuki, S. Sato, and T. Abe. Conceptual design and feasibility for a miniature Mars exploration rotorcraft. In *Proc. International Congress of the Aeronautical Sciences*, 2004.

[18] L. A. Young. Vertical lift – not just for terrestrial flight. In *Proc. AHS/AIAA/RaeS/SAE International Powered Lift Conference*, Arlington, VA, 2000.

[19] L. A. Young and E. W. Aiken. Vertical lift planetary aerial vehicles: Three planetary bodies and four conceptual design cases. In *Proc. European Rotorcraft Forum*, Moscow, Russia, 2001.

[20] L. A. Young, R. T. N. Chen, E. W. Aiken, and G. A. Briggs. Design opportunities and challenges in the development of vertical lift planetary aerial vehicles. In *Proc. American Helicopter Society International Vertical Lift Aircraft Design Conference*, San Francisco, CA, 2000.

[21] L. A. Young, E. W. Aiken, V. Gulick, R. Mancinelli, and G. A. Briggs. Rotorcraft as Mars scouts. In *Proc. IEEE Aerospace Conf.*, Big Sky, MT, 2002.

[22] L. A. Young, E. W. Aiken, and G. A. Briggs. Smart rotorcraft field assistants for terrestrial and planetary science. In *Proc. IEEE Aerospace Conference*, Big Sky, MT, 2004.

[23] L. A. Young, P. Lee, G. Briggs, and E. Aiken. Mars rotorcraft: Possibilities, limitations, and implications for human/robotic exploration. In *Proc. IEEE Aerospace Conference*, Big Sky, MT, 2005.

[24] L. A. Young et al. Use of vertical lift planetary aerial vehicles for the exploration of Mars. In *NASA Headquarters and Lunar and Planetary Institute Workshop on Mars Exploration Concepts*, Houston, TX, 2000.

[25] L. A. Young et al. Engineering studies into vertical lift planetary aerial vehicles. In *Proc. AHS International Meeting on Advanced Rotorcraft Technology and Life Saving Activities*, Utsunomiya, Tochigi, Japan, 2002.

[26] L. A. Young et al. Experimental investigation and demonstration of rotary-wing technologies for flight in the atmosphere of Mars. In *Proc. American Helicopter Society Annual Forum Proceedings*, Montreal, Canada, 2002.

© 2017. All rights reserved.